UCSF

Title

Tensor image enhancement and optimal multichannel receiver combination analyses for human hyperpolarized 13C MRSI

Permalink

https://escholarship.org/uc/item/3sv6p4v2

Journal

Magnetic Resonance in Medicine, 84(6)

ISSN

0740-3194

Authors

Chen, Hsin-Yu
Autry, Adam W
Brender, Jeffrey R
et al.

Publication Date

2020-12-01

DOI

10.1002/mrm.28328

Peer reviewed

Tensor image enhancement and optimal multichannel receiver combination analyses for human hyperpolarized 13C MRSI

Hsin-Yu Chen[1], **Adam W. Autry**[1], **Jeffrey R. Brender**[2], **Shun Kishimoto**[2], **Murali C. Krishna**[2], **Maryam Vareth**[1], **Robert A. Bok**[1], **Galen D. Reed**[3], **Lucas Carvajal**[1], **Jeremy W. Gordon**[1], **Mark van Criekinge**[1], **David E. Korenchan**[1], **Albert P. Chen**[3], **Duan Xu**[1], **Yan Li**[1], **Susan M. Chang**[4], **John Kurhanewicz**[1], **Peder E. Z. Larson**[1], **Daniel B. Vigneron**[1]

[1]Department of Radiology and Biomedical Imaging, University of California, San Francisco, California, USA

[2]Center for Cancer Research, National Cancer Institute, National Institutes of Health, Bethesda, Maryland, USA

[3]GE Healthcare, Chicago, Illinois, USA

[4]Department of Neurological Surgery, University of California, San Francisco, California, USA

Abstract

Purpose: With the initiation of human hyperpolarized ^{13}C (HP-^{13}C) trials at multiple sites and the development of improved acquisition methods, there is an imminent need to maximally extract diagnostic information to facilitate clinical interpretation. This study aims to improve human HP-^{13}C MR spectroscopic imaging through means of Tensor Rank truncation-Image enhancement (TRI) and optimal receiver combination (ORC).

Methods: A data-driven processing framework for dynamic HP ^{13}C MR spectroscopic imaging (MRSI) was developed. Using patient data sets acquired with both multichannel arrays and single-element receivers from the brain, abdomen, and pelvis, we examined the theory and application of TRI, as well as 2 ORC techniques: whitened singular value decomposition (WSVD) and first-point phasing. Optimal conditions for TRI were derived based on bias-variance trade-off.

Results: TRI and ORC techniques together provided a 63-fold mean apparent signal-to-noise ratio (aSNR) gain for receiver arrays and a 31-fold gain for single-element configurations, which particularly improved quantification of the lower-SNR-[^{13}C] bicarbonate and [1-^{13}C]alanine signals that were otherwise not detectable in many cases. Substantial SNR enhancements were observed for data sets that were acquired even with suboptimal experimental conditions, including delayed (114 s) injection (8× aSNR gain solely by TRI), or from challenging anatomy or geometry, as in the case of a pediatric patient with brainstem tumor (597× using combined TRI

and WSVD). Improved correlation between elevated pyruvate-to-lactate conversion, biopsy-confirmed cancer, and mp-MRI lesions demonstrated that TRI recovered quantitative diagnostic information.

Conclusion: Overall, this combined approach was effective across imaging targets and receiver configurations and could greatly benefit ongoing and future HP ^{13}C MRI research through major aSNR improvements.

Keywords

cancer imaging; hyperpolarized C-13 pyruvate; tensor rank truncation image enhancement

1 | INTRODUCTION

The development of hyperpolarized ^{13}C magnetic resonance imaging (HP ^{13}C MRI) has enabled an unprecedented means of accessing metabolic information noninvasively for cancer risk stratification and treatment monitoring.[1,2] Dynamic nuclear polarization of ^{13}C nuclei provides an approximately 50 000-fold increase in magnetic resonance signal, which provides 3-dimensional, real-time detection of cellular metabolic conversion.[3] As a 5-minute addition to a routine clinical MR exam, HP ^{13}C MRI has the potential to significantly advance clinical cancer research and individual patient management in the era of precision medicine.[1]

It has been known for nearly a century that the oncogenic upregulation of lactate dehydrogenase-driven pyruvate-to-lactate conversion, known as Warburg effect, is a hallmark of cancer.[4,5] Current HP ^{13}C MRI patient research monitors the kinetics of [1-^{13}C]pyruvate-to-[1-^{13}C]lactate conversion as a marker of cancer aggressiveness and a reporter of early response or resistance to targeted therapies.[1,6] Recent patient studies observed highly elevated pyruvate-to-lactate conversion in high-grade primary[7,8] and metastatic[9] prostate cancer, renal cell carcinoma,[10] breast cancer,[11] pancreatic adenocarcinoma,[12] and liver metastases.[13] A 4-fold decline of pyruvate-to-lactate conversion in a patient with castration-sensitive prostate cancer reflected androgen receptor signaling inhibition and early responses to treatment.[2]

Integrated into a standard-of-care, diagnostic-quality MRI exam, HP ^{13}C MR studies utilize specialized pharmaceutical manufacturing processes, a next generation human research polarizer, general purpose and target-specific coil designs, and efficient pulse sequences with the requisite spatiotemporal coverage and resolution.[1,6,8] As multisite HP ^{13}C studies expand, development of new coils and acquisition methods are still in progress, and there is a key unmet need to maximally extract the metabolic information from the acquired data sets. HP ^{13}C MRSI represents a family of acquisition strategies that provide good spatial coverage of the anatomy of interest and temporal sampling of kinetic profiles to capture metabolic information that reflect the in vivo biochemistry of ^{13}C-enriched probes.[7,8,14]

Enhancing HP data may benefit clinical interpretation and improve accuracy of kinetic model fits. Mathematically, the family of problems concerning compressed sensing, low-rank matrix completion, signal enhancement/denoising, and data compression have similar

basic ideas. All of these techniques are predicated on either the knowledge or assumption that the amount of information carried by a given data set is less than the theoretical "capacity" for its size and that the relevant information can be restructured into a simpler representation. Sometimes this concept is regarded as the "complexity" or "compressibility" of the data set, and in the context of HP-^{13}C MRSI is characterized by a finite and known numbers of resonances as well as a high degree of conformity over time (low rank in the dynamic and spectral dimensions). Deviations from this pattern usually correspond to noise and can be removed by techniques that deconstruct the image into simpler representations such as truncated singular value decomposition (SVD) and its higher dimensional analogs. Earlier work has shown appreciable performance from SVD based denoising,[15–21] the improvement of which was sufficient that glucose-to-lactate metabolism can be imaged using injected ^{13}C glucose with only thermal polarization.[22]

This project builds upon this prior preclinical work to develop a specialized HP ^{13}C dynamic MRSI processing framework for improving signal and noise characteristics in human studies to facilitate analysis. Specifically, it examines the theoretical foundations of the tensor Rank truncation—Image enhancement (TRI) technique on hyperpolarized human data, investigates rank relations and compressibility, and proposes an optimality condition to maximize the extraction of pathophysiological information (in the sense of information theory) in patient studies. As part of the effort, it also investigates the combination of data from ^{13}C receiver arrays using either whitened SVD (WSVD) or free induction decay first-point phasing (FPphasing). Optimization was evaluated on dynamic MRSI data sets from brain, abdomen, and pelvis using multichannel coil arrays and single-element receiver configurations. This new processing framework could benefit the data analysis for current and future clinical HP ^{13}C trials.

2 | METHODS

2.1 | Data processing framework in HP ^{13}C MR spectroscopic imaging

A renovated processing framework for HP ^{13}C MRSI is proposed in Supporting Information Figure S1. The new framework aims to provide refinements tailored to current and future multicenter clinical studies. Briefly, this entails noise decorrelation (prewhitening) of the MR array data, echo-planar spectroscopic imaging reconstruction with even-odd lobe phasing, B_0 correction, WSVD channel combination,[23] TRI by high-order singular value decomposition (HOSVD), and finally phase-sensitive peak estimation. Metabolites are quantified by area under phased peak. Built upon the fundamentals of processing and visualization from previous publications,[24,25] this work specifically focuses on implementing and evaluating the receiver channel combination and TRI techniques of the processing framework.

2.2 | Phase-sensitivity receiver array combination

HP experiments pose special challenges for MR receiver arrays. Contrary to radar and ultrasound arrays where the phase between elements carries indispensable information,[26] the phase differences between array receiver elements in MRI is a complicating factor that requires equalization. The premises of equalized receiver combination and some possible

techniques have been previously described in literature in the context of both proton[23] and nonproton nuclei.[27] Two array combination methods—WSVD and FPphasing—were compared in our study to find the best synergy with the proposed TRI techniques for optimal HP-^{13}C MRSI data processing, whose theory and application have previously been discussed for ^{1}H MRSI studies of brain tumors.[23]

2.3 | Tensor image enhancement of HP ^{13}C MRSI data

2.3.1 | Representation of HP ^{13}C MR data as tensors—In multilinear algebra, tensor is simply defined as a matrix of high dimensionality. Indeed, HP ^{13}C MRSI data, consisting of spectral, spatial, and dynamic dimensions, can be formulated into tensor representation. The formulation of HP ^{13}C MRSI tensors is described in Supporting Information Methods A (Illustrated in Supporting Information Figure S2).

2.3.2 | Compressibility in ^{13}C pyruvate-lactate dynamics, spectrum, and space—In a HP tensor, the metabolic conversion dynamics, chemical shift spectrum, and geometric space are inherently low rank. The validation and reasoning of low-rank properties in respectively.

2.3.3 | Formation of image space from rank-1 tensors—As a multidimensional tensor is hard to visualize, it is helpful to first consider a simplified data set with only 1 spatial dimension x (Supporting Information Figure S3).

$$\mathbb{M} = [\mathbb{G}; \mathbf{F}, \mathbf{X}, \mathbf{D}] = \sum_{p=1}^{P} \sum_{q=1}^{Q} \sum_{r=1}^{R} g_{pqr} \cdot \mathbf{f}_p \circ \mathbf{x}_q \circ \mathbf{d}_r \tag{1}$$

where $\mathbb{M}$ is the image tensor, $\mathbb{G}$ is the core tensor, and $\mathbf{F}$, $\mathbf{X}$, $\mathbf{D}$ and $\mathbf{f}$, $\mathbf{x}$, $\mathbf{d}$ stand for factor matrices and fibers in the spectral, spatial, and dynamic dimensions, respectively.

$$\text{Elementwise,} \quad \boldsymbol{m}_{ijk} = \sum_{p=1}^{P} \sum_{q=1}^{Q} \sum_{r=1}^{R} g_{pqr} f_{ip} x_{jq} d_{kr}.$$

Suppose there were a hypothetical HOSVD that only breaks down frequency and dynamic dimensions into principal component fibers but leaves the spatial dimension intact. In this case, the spatial factor matrix $\mathbf{X}$ becomes identity (each fiber $\mathbf{x} = \mathbf{e_q}$), namely $\mathbb{M} = [\mathbb{G}; \mathbf{F}, \mathbf{I}, \mathbf{D}]$. This gives

$$\boldsymbol{m}_{ijk} = \sum_{p=1}^{P} \sum_{r=1}^{R} g_{pjr} f_{ip} d_{kr} \tag{2}$$

Equation (2) suggests at spatial location j, the dynamic spectra of the voxel $\mathbf{M_j} = m(f, x = j, d)$ consists of the outer product of each $\mathbf{f_p}$ and $\mathbf{d_r}$, weighted by core tensor element g_{pjr}, and summed over p and r. For instance (Supporting Information Figure S3B), $\mathbf{f_1} \circ \mathbf{d_1}$ means that the dynamic spectra follow the spectral lineshape of the main pyruvate peak $\mathbf{f_1}$ and a single

dynamic profile $\mathbf{d_1}$. Recall $\mathbf{d_1}$ is the most dominant dynamic component extracted by HOSVD, which probably resembles pyruvate dynamics. In another word, voxel $\mathbf{M_j}$ is synthesized by the weighted sum of a collection of dynamic spectra $\mathbf{f_p} \circ \mathbf{d_r}$ (Supporting Information Figure S3C), where the weighting is stored in a slab $\mathbf{G_j}$ of the 3D core tensor $\mathbb{G}$. Mathematically, fibers $\mathbf{f_p}$ and $\mathbf{d_r}$ are analogous to the eigenvectors, and g_{pjr} is a generalization of singular value (Supporting Information Table).

Consequently, the low-rankness in spectral and dynamic dimensions means that any metabolite dynamics can be represented by a linear combination of $[\mathbf{d_1}, \mathbf{d_2}, \mathbf{d_3}, ..., \mathbf{d}_{\rho_D}]$ and any spectral peak by $[\mathbf{f_1}, \mathbf{f_2}, \mathbf{f_3}, ..., \mathbf{f}_{\rho_F}]$, where ρ_D and ρ_F are the dynamic and spectral ranks, respectively. This leads to a key property that voxel $\mathbf{M_j}$ can be fully synthesized with factor matrices $\mathbf{F}$ and $\mathbf{D}$ truncated to length ρ_F and ρ_D, and slab $\mathbf{G_j}$ truncated to size $\rho_F \times \rho_D$, respectively. As this holds true for any spatial index j, the entire image $\mathbb{M}$ (Supporting Information Figure S3D) can be fully represented by truncated $\mathbf{F}$, $\mathbf{D}$ and $\mathbb{G}$.

This example illustrated a barebones version of the multilinear SVD analysis, followed by image synthesis from rank-1 tensors. In the actual HP-MRI tensor decomposition, HOSVD extracts principal components in space into factor matrices $\mathbf{X}$, $\mathbf{Y}$, rather than leaving them identity. Nevertheless, the idea remains much the same despite decomposition in space and augmented dimensionality.

2.3.4 | Optimality condition for tensor low-rank thresholding—In order to maximally extract diagnostic information, Supporting Information Methods E derives the optimal conditions for tensor rank truncation based on bias-variance trade-off. Briefly, the optimization problem can be formulated as

$$\underset{\rho_1, \rho_2, ...\rho_i, ...\rho_D}{\text{argmin}} \frac{1}{K} \sum_k \left| \hat{S}_{\text{met,orig}}(k) - \hat{S}_{\text{met,TRI}}(k) \right|^2 + \sigma_{noise,TRI}^2 \tag{3}$$

where ρ_i is the rank in the i-th dimension, $\hat{S}_{\text{met}}(k)$ is the noisy estimate of metabolite signal from the k-th highest signal-to-noise ratio (SNR) voxel, and $\sigma_{\text{noise, TRI}}^2$ is the noise variance calculated from the free induction decay tail post rank truncation. The rank selection was based on the aforementioned criteria, calculated individually for each data set, and did not rely on *a priori* pathophysiological or other knowledge.

2.4 | MR experiments

The patient data (N = 38) examined in this study (Figures 1–8) were acquired using a 2D dynamic MRSI sequence,[8] following injection of 250 mM HP-[1-^{13}C]pyruvate, which was polarized using a 5T SPINlab (GE Healthcare, Chicago, IL). The sequence consisted of a multiband spectral-spatial excitation of a single slice, followed by symmetric echo-planar spectroscopic imaging readout (pulse repetition time/echo time [TR/TE] = 130/3.5 ms, resolution temporal = 2–5 s, 20–24 time points, spatial = 1.2–2 cm in-plane, 1.5–4 cm thick). Figure 1 summarized the ^{13}C receivers in this study. The brain studies utilized a clamshell transmitter together with custom-built 8-channel (UCSF) bilateral receivers or a birdcage transmitter in combination with a 32-channel array (UCSF-MGH).[28] The

abdominal scans utilized either a clamshell transmit/16-channel array receiver configuration (Rapid Biomedical, Rimpar, Germany), or an in-house figure-eight surface TR coil. The prostate setup consisted of a clamshell transmitter and a ^{1}H-^{13}C dual-element endorectal receiver.[7,8] All patient recruitment and human studies followed protocols approved by the internal review board at UCSF.

2.5 | Data analysis

Apparent SNR (aSNR) was calculated as maximum pyruvate peak divided by a spectrally resonance-free region on the edge of image outside subject. The pyruvate-to-lactate conversion rate (k_{PL}) was evaluated using an inputless 2-site exchange model.[29]

Algorithm implementations, data processing, visualizations, and simulations were performed on Matlab (The MathWorks, Natick, MA) and open-source SIVIC software.[24] The Matlab and Python programming codes used in this study can be found in Hyperpolarized MRI Toolbox, https://github.com/LarsonLab/hyperpolarizedmri-toolbox.

The programs are licensed under CC BY-NC-SA 4.0.

3 | RESULTS

3.1 | HP ^{13}C data tensor is low-rank in dynamic dimension

A data-driven simulation, with methodologies described in Supporting Information Methods B and outcomes in Supporting Information Results A, illustrates that the dynamics of pyruvate, lactate, and other downstream metabolites can be described by a low-rank basis $\overline{D}$ (Supporting Information Figure S5).

3.2 | Phase-sensitive channel combination allows more accurate detection of downstream metabolites

The FPphasing and WSVD techniques were compared to the naive sum-of-squares (SOS). WSVD and FPphasing resulted in Gaussian zero-mean noise (Figure 2), whereas simple SOS yielded Rician noise with nonzero mean. Both channel combination techniques provided qualitatively and quantitatively comparable performance, substantially reducing noise baseline over SOS and highlighting lactate/alanine in kidneys/muscle relative to background (Figures 2 and 3). The data also implied they are relatively robust to breathing motion. The following results utilized WSVD by default unless otherwise specified.

3.3 | WSVD and TRI improves aSNR by an order of magnitude or more and recovers otherwise undetectable metabolites

Mean aSNR gain (Figure 1) for the combined use of TRI and WSVD was 63-fold for arrays and 31-fold for single-element receivers in different imaging targets and coil set ups, where at least a minimum 10-fold improvement can be expected for arrays.

The results were consistent across multiple imaging targets and reveal in many cases previously undetected details. In Figures 4–6, TRI was independently evaluated using single coil (liver, prostate) or channel combined (brain) data. Figure 4A depicts data from a patient

diagnosed with rectosigmoid cancer liver metastasis. A hypoenhancing liver lesion was identified on the contrast MR in segment 7 (red arrow), measuring 3.8×2.4 cm. The information optimality selected rank $(\rho_F, \rho_X, \rho_Y, \rho_D) = (12, 9, 10, 11)$ out of a data matrix size of (59, 16, 18, 18), offering a 13-fold aSNR gain. Although the effect of the aSNR gain was not immediately obvious in the high SNR pyruvate images, the liver parenchyma and lesion became more conspicuous in the lactate TRI image, and the distinctive portal venous phase (indicated by the green arrow) was preserved by TRI. Figure 4B shows a data set from a brain tumor case (oligoastrocytoma) with relatively low raw SNR due to a long injection delay (114 s). Employing TRI with the optimum rank of (13, 7, 11, 8) from a data matrix size (59, 10, 18, 24) resulted in an 8-fold aSNR gain, sufficient to recover the bicarbonate signal, which was at noise level in the absence of TRI.

Figures 5 and 6 depicts a patient diagnosed with biopsy-confirmed bilateral prostate cancer in left, right midg-land, and right apex. Figure 5 highlights a T_2 hypointensity and corresponding ^{13}C voxel in green. The post-TRI image shows gain of apparent SNR in pyruvate, lactate, and even recovery of otherwise undetectable alanine and pyruvate-hydrate. Overall apparent SNR gain was 67-fold in this data set. Dynamic series of pyruvate and lactate in Figure 6A illustrated improved spatiotemporal characteristics, especially for lactate signal. This resulted in dynamic profiles consistent with what is typically observed in human prostate,[8] and, therefore, more reliable pyruvate-to-lactate conversion rate k_{PL} fits over the prostate, as shown in Figure 6B. The fitting error metric[30] also indicated that the error decreased and the accuracy increased after TRI. Diffusion images were unavailable for this study. Spatiotemporal "imprinting" of high SNR signals onto lower SNR signals, a common concern for low-rank denoising methods, was not observed in any of these examples.

Figure 7 illustrated the synergy between TRI and WSVD channel combination in a pediatric HP-^{13}C exam targeting the brainstem. For patient safety, the [1-^{13}C] pyruvate dose and injection rate had to be reduced from the standard values per study protocol. Intrinsic SNR was poor using simple SOS combination, imposing challenges for lactate analysis. Comparison of the optimized data processing versus the original revealed a 597-fold aSNR gain. Upon closer examination, the aSNR gain from WSVD array combination was ~7-fold, whereas ~88-fold of the improvement was attributed to TRI. In this example, a snapshot at time point 5 (Figure 7B) showed substantially improved spectral characteristics and even the recovery of some spatial Gibbs ringing artifact that was buried in the noise.

In addition to the human data, a simulated validation of TRI was described in Supporting Information Results B and Supporting Information Figure S7.

3.4 | Optimal rank selection is essential to TRI

Figure 8 (detailed in Supporting Information Figure S4) use TRI with different ranks to illustrate the compromise between bias and variance in a sample brain data set. Insufficient spectral rank led to poor representation of the ^{13}C metabolite peak profiles, thereby biasing peak quantification (Supporting Information Figure S4B). Too low dynamic rank resulted in departure of dynamic curves from truth, again creating bias. These undesirable characteristics can be mitigated by selecting rank based on the bias/variance optimum

described in Equation (3) (Figure 8A). The diagram in Figure 8A illustrates the cost function for different degrees of TRI: weak TRI leads to higher variance, whereas strong TRI leads to higher bias. The optimality condition minimizes the cost function, defined as the sum of bias and variance.

4 | DISCUSSION

4.1 | Tensor image enhancement and optimal receiver arrays

The TRI technique is data driven and makes little assumption about chemical shifts, line profiles, spatial features, or dynamic characteristics of HP ^{13}C MRSI data. Instead, the HOSVD implicitly extracts these attributes from the observation, and the rank truncation compresses the image into a simpler representation that strengthens the pathophysiological interpretation of the information content. This contrasts with many current signal enhancement techniques that require prior information in the form of a predefined dictionary of images[16] or predetermined functional form. Indeed, this feature is particularly important for HP ^{13}C MRSI as clinical studies are currently still in early phase and an extensive human database is not yet available. No assumptions are made in HOSVD about smoothness in any dimension,[31] allowing the accurate reconstruction of high-resolution features. This data-driven approach greatly increases TRI's versatility, as demonstrated in its effectiveness in a broad range of cancer applications in the brain, prostate, and liver utilizing different transmit/receive hardware configurations.

Although many signal enhancement and denoising methods are beset by either the "imprinting" of high SNR signals onto those with low SNR or the complete loss of low SNR signals,[32] this was not observed with TRI. From the patient examples evaluated in this work, pyruvate and lactate were accordingly found to have distinct spatial distributions and dynamic profiles (Figures 4–7). It is also important to understand whether application of TRI generated excessive artifacts in exchange for desirable aSNR gain. This question was addressed by the case in Figures 5 and 6, which demonstrated that post-TRI k_{PL} modeling yielded better accuracy to characterize biopsy-confirmed cancer. This strongly suggested that quantitative pathological information can be recovered without being dominated by artifacts.

The synergy between TRI and optimal MR array signal combination is best exemplified by detecting low abundance metabolites. The optimal channel combination using either WSVD or FPphasing provided zero-mean Gaussian noise statistics. In the simple SOS combination, the low-SNR peaks reside on a noise floor with a positive mean, which creates a significant positive bias in k_{PB} estimation and in the associated metabolite ratios. It highlights a key utility to quantifying relatively low-SNR metabolites such as bicarbonate and alanine and to some extent lactate. Low SNR metabolites such as bicarbonate may inform on disease state and progression in glioblastoma[14] and is a pivotal biomarker for probing mitochondrial oxidative phosphorylation. Improving aSNR and noise statistics helps overcome this hurdle. The proposed framework is particularly advantageous for analyzing human data sets with low SNR owing to delayed injection (Figure 4B) or anatomy that is challenging to image (Figure 7), situations that are often encountered during the technology development phase of HP ^{13}C MRI. Recovery of low SNR resonances without a priori knowledge of the chemical

shifts of reaction products suggests that this framework may also facilitate HP probe discovery in proof-of-concept studies, where low polarization, slow conversion, or short T_1 of the initial lead compound may prove obstacles to further development.

4.2 | Why TRI is more appropriate than conventional SVD in dynamic HP ^{13}C MRSI?

In the limiting case of 2 dimensions, De Lathauwer et al showed that HOSVD degenerates to a conventional SVD (Theorem 1 and 2 in Ref. 33). The factor matrices $\mathbf{U}^{(1)}$ and $\mathbf{U}^{(2)}$ become left and right singular matrices $\mathbf{U}$ and $\mathbf{V}$ that contain left and right singular vectors, respectively, and the core tensor $\mathbb{G}$ degenerates to the diagonal singular value matrix . In this scenario, the number of ^{13}C resonances equals the number of distinct dynamics; equivalently, the spectral rank ρ_F equals dynamic rank ρ_D. Rank truncation in SVD can easily be accomplished by simply dropping singular values, because is diagonal. The conventional SVD technique is a natural representation for nonimaging time-resolved spectroscopy experiments and, therefore, holds importance for applications in HP bioreactor[34,35] and in vivo spectrometer studies.[36]

The dynamic spectroscopy case further illustrated why tensor decomposition is an appropriate structure to represent HP ^{13}C MRSI data that has spectral, spatial, and dynamic dimensions. Rather than being diagonal as in 2D SVD, the high-dimensional core tensor $\mathbb{G}\left(\mathbb{G} \in \mathbb{C}^{P \times Q \times S \times R}\right)$ is a full tensor, meaning that each of its elements can take on a nonzero value. Unlike the conventional SVD case, where the row and column ranks are automatically equal, the core tensor can be truncated to a different degree in each dimension. The core tensor $\mathbb{G}$, in conjunction with factor matrices $\mathbf{F}$, $\mathbf{X}$, $\mathbf{Y}$, and $\mathbf{D}$, provides the necessary degrees of freedom to fully describe the spatiotemporal complexity of the HP data set.

4.3 | How to apply optimality condition in practice?

In the conventional SVD context, the best rank-r approximation of the data matrix is simply formed using the truncated version of the singular value matrix and singular vector matrices $\mathbf{U}$, $\mathbf{V}$ to rank r. This is known as the Eckart-Young-Mirsky theorem.[37] Although many theorems and properties in 2D SVD find their high-order analogy in HOSVD, Chen et al pointed out that Eckart-Young-Mirsky relations cannot be directly generalized to high-order tensor decomposition.[38] Fortunately, De Lathauwer et al and Kolda et al[39,40] established that quasi-optimal solutions exist for low-rank approximation for HOSVD. Many HOSVD algorithms and approximations,[41] including the ST-MLSVD[42] used in this study, are readily available to obtain a quasi-optimal solution that is satisfactory for practical scientific and engineering applications.

This approximation of optimum may explain why the estimated value of cost function (3) is not strictly convex in the region near global minimum. However, the results from human data suggested that the enhanced HP ^{13}C MRSI data are quantitatively and qualitatively insensitive to small deviations from global minimum, in terms of metabolite distribution and k_{PL} estimates. Examination of the estimated cost function also revealed that it exhibits a plateau near optimality, indicating its convergence and that a desirable approximation can be achieved.

Admittedly, brute-force mapping of the cost function for each n-rank combination is computationally expensive, having complexity $O (P \times Q \times R \times \ldots)$. For the MRSI human data presented in this study, calculation of the cost function takes ~20 minutes. However, this time can increase considerably when dealing with higher dimensional data. Most convex optimization algorithms do require strict convexity to search for the global minimum. One idea is to optimize (3) using cutting-edge machine learning techniques.[43,44] Another option is to implement HOSVD on graphic processors to calculate the possible rank combinations for (3) in parallel.

4.4 | Clinical imaging targets

The "compressibility" in n-th dimension, reflected by the n-rank, of the data tensor is automatically determined based on bias-variance trade-off. Typically, the spectral and dynamic dimensions are more compressible than the spatial dimensions. Some observation can be made regarding the rank selection for different imaging targets. As was described in the Methods section, the spatial rank could depend on the anatomical structure of the target, and the ^{1}H reference scans may provide a general idea what the complexity and, therefore, compressibility is. However, it is still noteworthy that a functional scan like ^{13}C does not necessarily have the same underlying complexity as proton images. For brain imaging, the spatial support is usually the head size, whereas that for abdomen and prostate is normally the receiver sensitivity profile of surface and endorectal receivers, respectively. A curious observation is that if the 2 hemispheres were perfectly symmetric, y-rank $\rho_Y \approx S/2$; but they never are in practice.

The f-rank is largely determined by the number of independent metabolites and their line profiles. In [1-^{13}C]pyruvate studies, pyruvate, pyruvate-hydrate, lactate, bicarbonate, and alanine are commonly observed. Generally speaking, larger imaging targets such as the abdomen or whole pelvis tend to have less ideal shims.

Compressibility in dynamics is a function of hemodynamical heterogeneity in the target region. Accordingly, the more distinct pyruvate dynamic characteristics necessitate a larger basis set. The higher d-rank would also apply to account for the 2 hepatic phases. Pathologically, hepatocellular carcinoma and many liver metastases receive a majority of their blood supply from the hepatic artery, whereas parenchyma is primarily perfused by the portal vein.[45–47] Sensibly, more fibers $\mathbf{d_r}$ are required to sufficiently describe arterial and portal venous phases.

4.5 | Can this technique be generalized to HP ^{13}C MRI acquisition and reconstruction strategies?

Functionally, this TRI and denoising should be applicable to many different clinical acquisition schemes. Although the resonance-specific imaging sequences, such as echo-planar imaging, lack the highly compressible spectral dimension, they have compressibility in the spatial and dynamic dimensions similar to the MRSI sequence. Therefore, TRI is expected to offer moderate SNR enhancement for these imaging-based sequences. One potential approach for echo-planar imaging is to bundle lactate and other products together and perform a joint rank truncation. For instance, first reformulate the lactate image $\mathbf{L}$(x, y,

d) and bicarbonate image $\mathbf{B}(x, y, d)$ into $\mathbf{P}(2, x, y, d)$, and then, compress in dynamics. This follows Observation III (Supporting Information Methods B) where pyruvate products share the same dynamic fibers. An example is presented in Supporting Information Figure S6.

With regard to acquisition strategies, it is worth noting that—although each dimension has some degree of compressibility, some dimensions are inherently more compressible. For TRI, it may be beneficial to acquire the highly compressible spectral and dynamic dimensions. Consequently, a 2D/3D dynamic MRSI data set may have higher TRI power than 2D conventionally encoded chemical shift imaging or 3D metabolite-specific imaging schemes. However, coverage of each dimension, in terms of extent and resolution, comes at the cost of acquisition time, which entails depletion of valuable HP magnetization. Although TRI may improve this trade-off, it is important to tailor a sequence to acquire the most relevant information for achieving a specific diagnostic goal, whether fine spatial details and features, pyruvate-lactate kinetics, or spectral characteristics.

An interesting application in this respect is perhaps pseudo-randomly undersampled acquisition sequences, such as 3D compressed sensing-echo-planar spectroscopic imaging[48] or SAKE echo-planar imaging[49] sequences. First, the sampling density could be redesigned to reflect compressibility in each dimension. Concurrently, TRI could be implemented either as a reconstruction algorithm or serve as a penalty term to k-space interpolation.

4.6 | Data-driven vs model-based denoising approaches

Model-based denoising approaches such as linear combination model or generalized linear model analyze spectra and temporal dynamics using predefined regressors.[50] This type of technique can be advantageous when the patient ^{13}C database is sufficiently large to derive spectral and dynamic regressors based on, for instance, population mean. The data-driven TRI reported in our work may be beneficial when limited numbers of patient data sets are available, because the principal components are directly derived from each data set itself without reliance on predefined components. The comparison of model-based vs model-free methodologies will be of future interest.

4.7 | Potential limitations

Optimal rank selection would ideally provide a rank estimate that maximizes usable information content. It is still conceptually important to realize that compression and rank truncation promote overall commonality across the data set, and oversimplification of the data set could weaken the distinction between normal and disease metabolism. Additionally, rank reduction in D could modulate pyruvate dynamics (Supporting Information Figure S5C), and thereby alter perfusion characteristics, despite its negligible impact on the metabolic rate constant k_{PL} (Supporting Information Figure S5D).

Another constraint is the lack of a gold standard to investigate and further optimize TRI. Because of the transient nature of HP ^{13}C magnetization and finite encoding speeds, it is challenging to acquire a high-SNR "gold standard" data set for carbon as in proton MRI. Existing physical and numerical phantoms do not adequately reflect the spatiotemporal complexity and coherence of carbon pharmacokinetics and molecular interactions in

humans. As our understanding of human metabolic pathophysiology improves through clinical trials, such knowledge will help benchmark relevant techniques under development.

5 | CONCLUSIONS

This data-driven processing framework for dynamic HP ^{13}C MRSI utilized optimal receiver-array combination and tensor image enhancement to substantially improve extraction of diagnostic information in a variety of human cancer applications. This could significantly benefit ongoing and future HP ^{13}C-pyruvate MRI studies, as well as new HP probe discovery and translation.

Supplementary Material

Refer to Web version on PubMed Central for supplementary material.

ACKNOWLEDGMENTS

REFERENCES

1. Kurhanewicz J, Vigneron DB, Ardenkjaer-Larsen JH, et al. Hyperpolarized (13)C MRI: Path to clinical translation in oncology. Neoplasia. 2019;21:1–16. [PubMed: 30472500]

2. Aggarwal R, Vigneron DB, Kurhanewicz J. Hyperpolarized 1-[(13)C]-pyruvate magnetic resonance imaging detects an early metabolic response to androgen ablation therapy in prostate cancer. Eur Urol. 2017;72:1028–1029. [PubMed: 28765011]

3. Ardenkjaer-Larsen JH, Fridlund B, Gram A, et al. Increase in signal-to-noise ratio of >10,000 times in liquid-state NMR. Proc Natl Acad Sci USA. 2003;100:10158–10163. [PubMed: 12930897]

4. Hsu PP, Sabatini DM. Cancer cell metabolism: Warburg and beyond. Cell. 2008;134:703–707. [PubMed: 18775299]

5. Ward PS, Thompson CB. Metabolic reprogramming: A cancer hallmark even Warburg did not anticipate. Cancer Cell. 2012;21:297–308. [PubMed: 22439925]

6. Wang ZJ, Ohliger MA, Larson PEZ, et al. Hyperpolarized (13)C MRI: State of the art and future directions. Radiology. 2019;182391.

7. Chen HY, Larson PEZ, Gordon JW, et al. Technique development of 3D dynamic CS-EPSI for hyperpolarized (13) C pyruvate MR molecular imaging of human prostate cancer. Magn Reson Med. 2018;80:2062–2072. [PubMed: 29575178]

8. Nelson SJ, Kurhanewicz J, Vigneron DB, et al. Metabolic imaging of patients with prostate cancer using hyperpolarized [1-C-13]pyruvate. Sci Transl Med. 2013;5:198ra108.

9. Chen H-Y, Aggarwal R, Bok RA, et al. Hyperpolarized 13 C-pyruvate MRI detects real-time metabolic flux in prostate cancer metastases to bone and liver: A clinical feasibility study. Prostate Cancer Prostatic Dis. 2019;1–8.

10. Tran M, Latifoltojar A, Neves JB, et al. First-in-human in vivo non-invasive assessment of intra-tumoral metabolic heterogeneity in renal cell carcinoma. BJR|Case Reports. 2019;5(3):20190003. [PubMed: 31428445]

11. Gallagher FA, Woitek R, McLean MA, et al. Imaging breast cancer using hyperpolarized carbon-13 MRI. Proc Natl Acad Sci. 2020;117:2092–2098. [PubMed: 31964840]

12. Stodkilde-Jorgensen H, Laustsen C, Hansen ESS, et al. Pilot study experiences with hyperpolarized [1-(13) C]pyruvate MRI in pancreatic cancer patients. J Magn Reson Imaging. 2020;51:961–963. [PubMed: 31368215]

13. Zhu Z, Marco-Rius I, Ohliger MA, et al. Hyperpolarized 13C dynamic breath-held molecular imaging to detect targeted therapy response in patients with liver metastases. Proceedings of the International Society for Magnetic Resonance in Medicine, Concord CA, 2017 25th Annual Meeting, Abstract Number 1115.

14. Park I, Larson PEZ, Gordon JW, et al. Development of methods and feasibility of using hyperpolarized carbon-13 imaging data for evaluating brain metabolism in patient studies. Magn Reson Med. 2018;80:864–873. [PubMed: 29322616]

15. Kishimoto S, Brender JR, Crooks DR, et al. Imaging of glucose metabolism by 13C-MRI distinguishes pancreatic cancer subtypes in mice. Elife. 2019;8:e46312. [PubMed: 31408004]

16. Lam F, Li Y, Peng X. Constrained magnetic resonance spectroscopic imaging by learning nonlinear low-dimensional models. IEEE Trans Med Imaging. 2020;39:545–555. [PubMed: 31352337]

17. Liu Y, Ma C, Clifford BA, et al. Improved low-rank filtering of magnetic resonance spectroscopic imaging data corrupted by noise and B(0) field inhomogeneity. IEEE Trans Biomed Eng. 2016;63:841–849. [PubMed: 26353360]

18. Ma C, Clifford B, Liu Y, et al. High-resolution dynamic 31P-MRSI using a low-rank tensor model. Magn Reson Med. 2017;78: 419–428. [PubMed: 28556373]

19. Song JE, Shin J, Lee H, et al. Dynamic hyperpolarized 13C MR spectroscopic imaging using SPICE in mouse kidney at 9.4 T. NMR Biomed. 2019;e4230. [PubMed: 31856426]

20. Zhang X, Peng J, Xu M, et al. Denoise diffusion-weighted images using higher-order singular value decomposition. NeuroImage. 2017;156:128–145. [PubMed: 28416450]

21. Nguyen HM, Peng X, Do MN, Liang ZP. Denoising MR spectroscopic imaging data with low-rank approximations. IEEE Trans Biomed Eng. 2013;60:78–89. [PubMed: 23070291]

22. Brender JR, Kishimoto S, Merkle H, et al. Dynamic imaging of glucose and lactate metabolism by 13 C-MRS without hyperpolarization. Sci Rep. 2019;9:1–14. [PubMed: 30626917]

23. Vareth M, Lupo J, Larson P, Nelson S. A comparison of coil combination strategies in 3D multi-channel MRSI reconstruction for patients with brain tumors. NMR Biomed. 2018;31:e3929. [PubMed: 30168205]

24. Crane JC, Olson MP, Nelson SJ. SIVIC: Open-source, standards-based software for DICOM MR spectroscopy workflows. Int J Biomed Imaging. 2013;2013:1–12.

25. Nelson SJ, Li Y, Lupo JM, et al. Serial analysis of 3D H-1 MRSI for patients with newly diagnosed GBM treated with combination therapy that includes bevacizumab. J Neurooncol. 2016;130:171–179. [PubMed: 27535746]

26. Van Trees HL. Optimum Array Processing: Detection Estimation and Modulation Theory. Part IV Hoboken NJ: Wiley Interscience; 2002.

27. Stoll VM, Clarke WT, Levelt E, et al. Dilated cardiomyopathy: Phosphorus 31 MR spectroscopy at 7 T. Radiology. 2016;281:409–417. [PubMed: 27326664]

28. Autry AW, Gordon JW, Carvajal L, et al. Comparison between 8-and 32-channel phased-array receive coils for in vivo hyperpolarized 13C imaging of the human brain. Magn Reson Med. 2019;82:833–841. [PubMed: 30927300]

29. Larson PEZ, Chen H-Y, Gordon JW, et al. Investigation of analysis methods for hyperpolarized 13C-pyruvate metabolic MRI in prostate cancer patients. NMR Biomed. 2018;e3997. [PubMed: 30230646]

30. Mammoli D, Carvajal L, Slater JB, et al. Kinetic modeling of hyperpolarized carbon-13 pyruvate metabolism in the human brain. IEEE Trans Med Imaging. 2020;39:320–327. [PubMed: 31283497]

31. Hien MN, Haldar JP, Do MN, Liang ZP. Denoising of MR spectroscopic imaging data with spatial-spectral regularization. 2010 7th IEEE International Symposium on Biomedical Imaging: From Nano to Macro. 2010;720–723.

32. Donoho DL, Johnstone IM, Stern AS, Hoch JC. Does the maximum-entropy method improve sensitivity. Proc Natl Acad Sci USA. 1990;87:5066–5068. [PubMed: 11607089]

33. De Lathauwer L, De Moor B, Vandewalle J. A multilinear singular value decomposition. SIAM journal on Matrix Analysis and Applications. 2000;21:1253–1278.

34. Keshari KR, Sriram R, Van Criekinge M, et al. Metabolic reprogramming and validation of hyperpolarized 13C lactate as a prostate cancer biomarker using a human prostate tissue slice culture bioreactor. Prostate. 2013;73:1171–1181. [PubMed: 23532911]

35. Sriram R, Van Criekinge M, Hansen A, et al. Real-time measurement of hyperpolarized lactate production and efflux as a biomarker of tumor aggressiveness in an MR compatible 3D cell culture bioreactor. NMR Biomed. 2015;28:1141–1149. [PubMed: 26202449]

36. Najac C, Radoul M, Le Page LM, et al. In vivo investigation of hyperpolarized [1,3-(13)C2]acetoacetate as a metabolic probe in normal brain and in glioma. Sci Rep. 2019;9:3402. [PubMed: 30833594]

37. Eckart C, Young G. The approximation of one matrix by another of lower rank. Psychometrika. 1936;1:211–218.

38. Chen J, Saad Y. On the tensor SVD and the optimal low rank orthogonal approximation of tensors. Siam Journal on Matrix Analysis and Applications. 2008;30:1709–1734.

39. De Lathauwer L, De Moor B, Vandewalle J. On the best rank-1 and rank-(R1, R2,., R-N) approximation of higher-order tensors. Siam Journal on Matrix Analysis and Applications. 2000;21:1324–1342.

40. Kolda TG, Bader BW. Tensor decompositions and applications. Siam Review. 2009;51:455–500.

41. Grasedyck L, Kressner D, Tobler C. A literature survey of low-rank tensor approximation techniques. GAMM-Mitteilungen. 2013;36:53–78.

42. Vannieuwenhoven N, Vandebril R, Meerbergen K. A new truncation strategy for the higher-order singular value decomposition. Siam Journal on Scientific Computing. 2012;34:A1027–A1052.

43. Jain P, Kar P. Non-convex optimization for machine learning. Foundations and Trends in Machine Learning. 2017;10:142–336.

44. Zhang Y, Liang P, Wainwright MJ. Convexified convolutional neural networks. In: Proceedings of the 34th International Conference on Machine Learning-Volume 70. JMLR. org; 2017: 4044–4053.

45. Breedis C, Young G. The blood supply of neoplasms in the liver. Am J Pathol. 1954;30:969–977. [PubMed: 13197542]

46. Lin G, Lunderquist A, Hagerstrand I, Boijsen E. Postmortem examination of the blood supply and vascular pattern of small liver metastases in man. Surgery. 1984;96:517–526. [PubMed: 6474357]

47. Sigurdson ER, Ridge JA, Kemeny N, Daly JM. Tumor and liver drug uptake following hepatic artery and portal vein infusion. J Clin Oncol. 1987;5:1836–1840. [PubMed: 3681370]

48. Larson PEZ, Hu S, Lustig M, et al. Fast dynamic 3D MR spectroscopic imaging with compressed sensing and multiband excitation pulses for hyperpolarized 13C studies. Magn Reson Med. 2011;65:610–619. [PubMed: 20939089]

49. Feng Y, Gordon JW, Shin PJ, et al. Development and testing of hyperpolarized (13)C MR calibrationless parallel imaging. J Magn Reson. 2016;262:1–7. [PubMed: 26679288]

50. Monti MM. Statistical analysis of fMRI time-series: A critical review of the GLM approach. Front Hum Neurosci. 2011;5:28. [PubMed: 21442013]
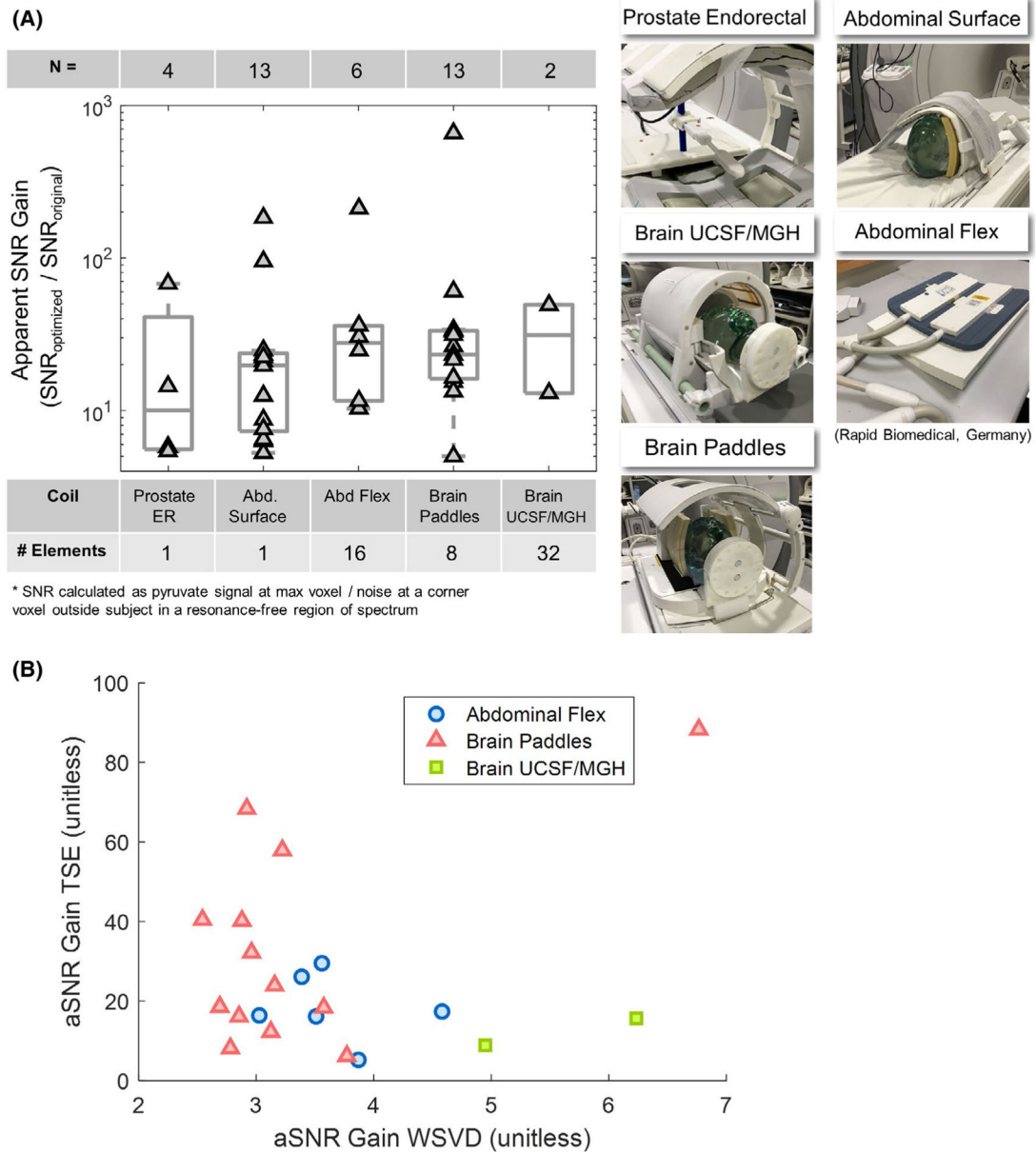
(A)

| N = | 4 | 13 | 6 | 13 | 2 |

Coil	Prostate ER	Abd. Surface	Abd Flex	Brain Paddles	Brain UCSF/MGH
# Elements	1	1	16	8	32

* SNR calculated as pyruvate signal at max voxel / noise at a corner voxel outside subject in a resonance-free region of spectrum

(B)

FIGURE 1.

A, The improved framework was evaluated on human hyperpolarized (HP) ^{13}C exams of brain, abdomen, and pelvis using a varietsy of coil configurations including multichannel array and single-element receivers. Mean apparent signal-to-noise ratio (aSNR) gain was 49-fold. B, Breakdown of aSNR gains from whitened singular value decomposition (WSVD) and Tensor Rank truncation-Image enhancement (TRI) per data set for each array imaging setup
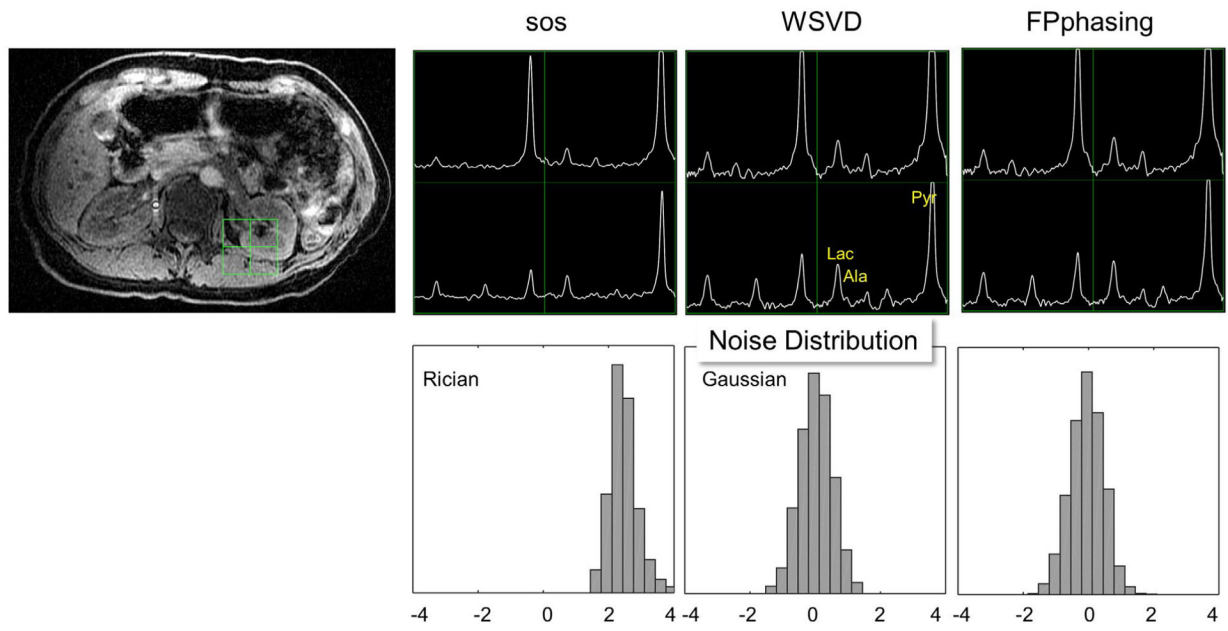
FIGURE 2.
Abdominal study on a healthy volunteer using the 16-channel flex array. The channels were combined using simple sumof-squares (SOS), or the 2 optimal channel combination methods – whitened singular value decomposition (WSVD) and first point phasing (FPphasing). No Tensor Rank truncation-Image enhancement (TRI) was applied. Both methods preserved phase characteristics and gave Gaussian zero-mean noise, whereas sos yielded Rician noise with nonzero mean. Improved signal-to-noise (SNR) and noise statistics are essential to probing human cancer metabolism, as they benefit k_{PL} estimation by improving quantification of relatively low-SNR lactate and alanine. The performance of WSVD vs FPphasing was comparable
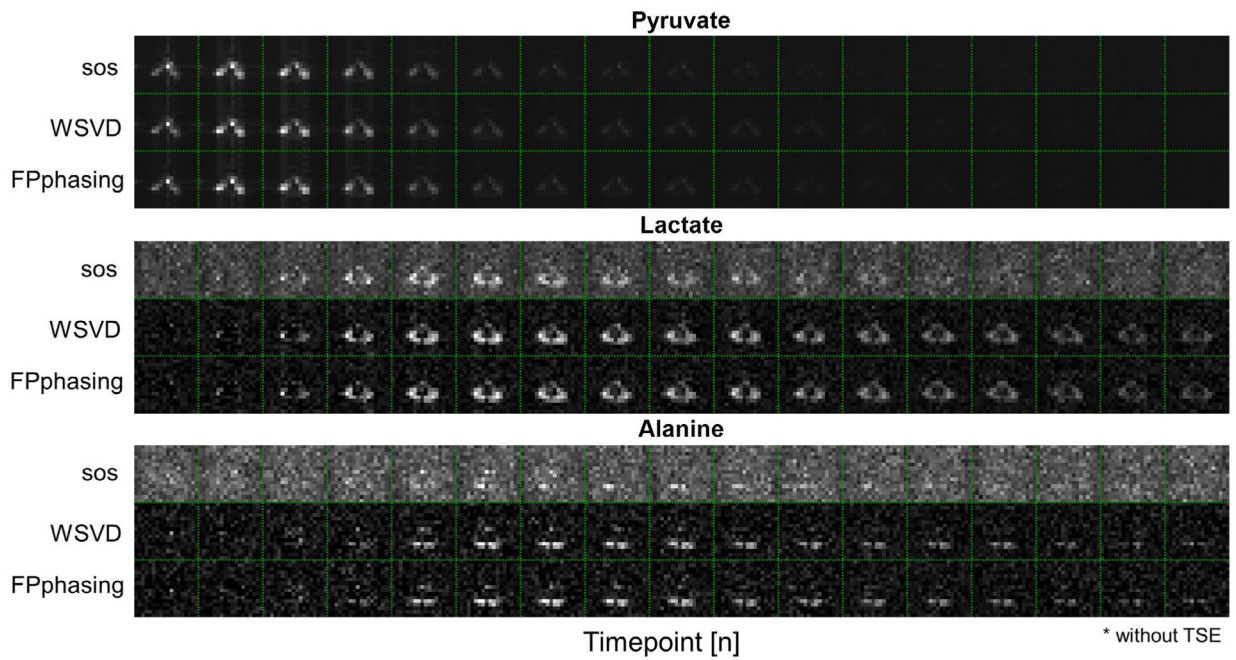
FIGURE 3.
This is a continuation of Figure 2. The optimal combinations provided substantially reduced noise baseline over sum-of-squares (SOS), highlighting lactate/alanine in kidneys/muscle versus background. The findings implied they are relatively robust to breathing motion
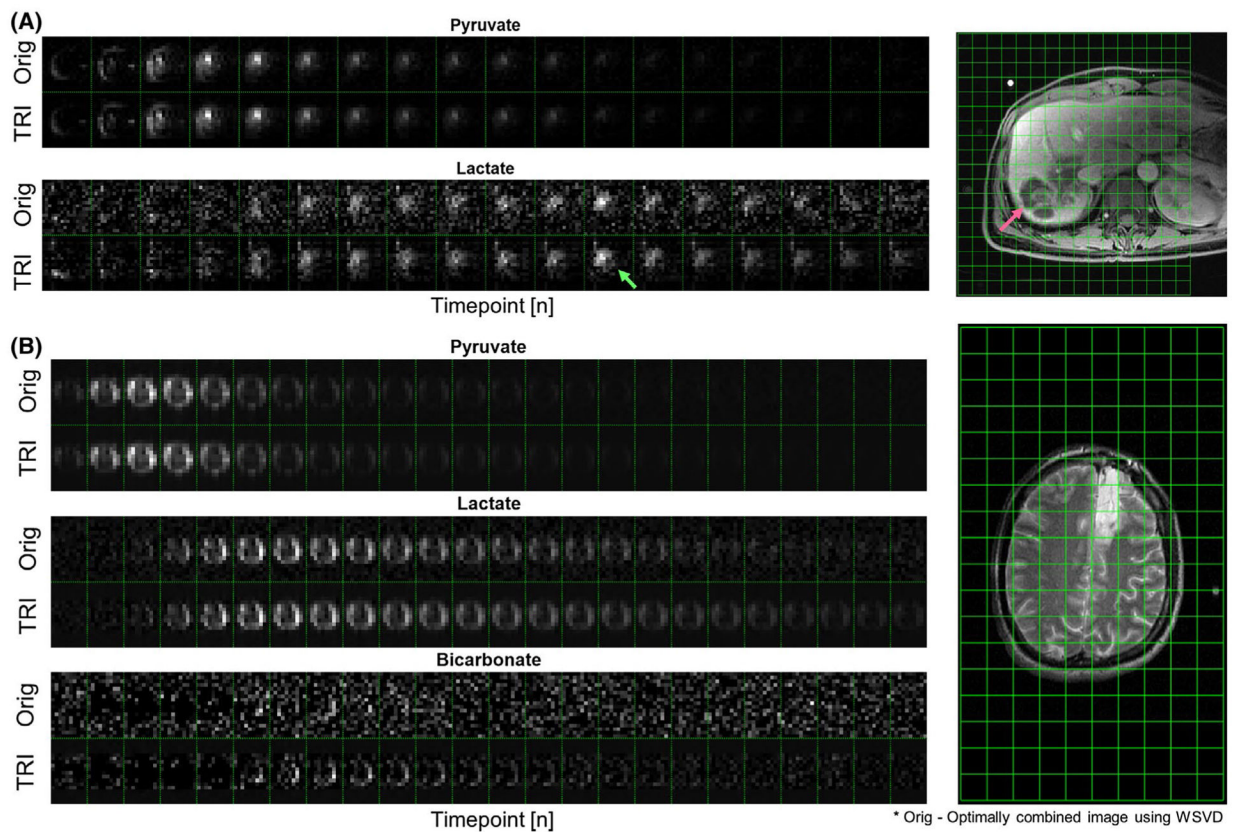
FIGURE 4.
Validation of Tensor Rank truncation-Image enhancement (TRI) on various imaging targets illustrating different human hyperpolarized (HP) ^{13}C image targets of different structure and complexity, and how the optimality condition provides adaptive rank estimation. A, This case of rectosigmoid cancer was identified with a liver metastasis in segment 7 (red arrow). Information optimality resulted in 13× apparent signal-to-noise (aSNR) gain. Note portal venous phase on dynamics (green arrow). A slight contamination of urea phantom was likely due to spectral baseline. B, In this brain tumor case, TRI provided 8× aSNR gain with recovery of [^{13}C]bicarbonate
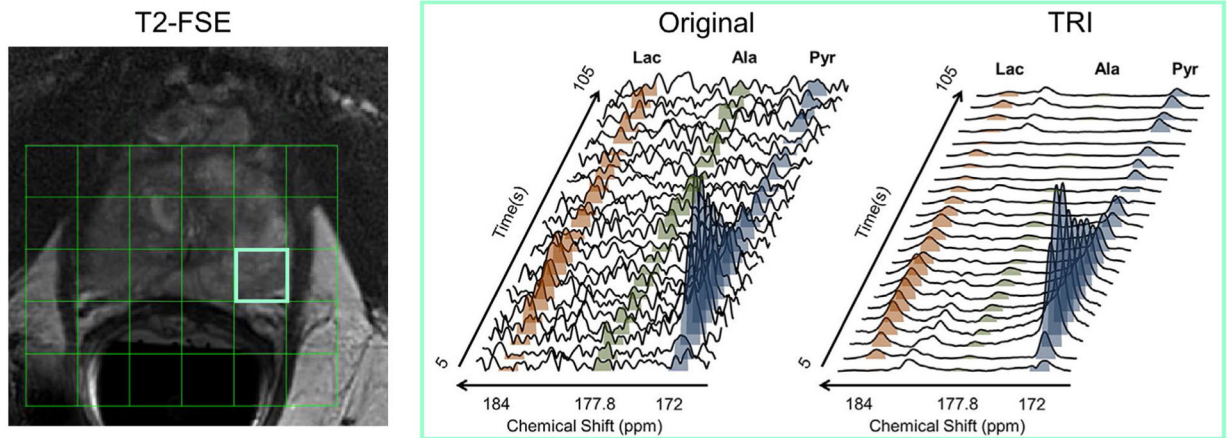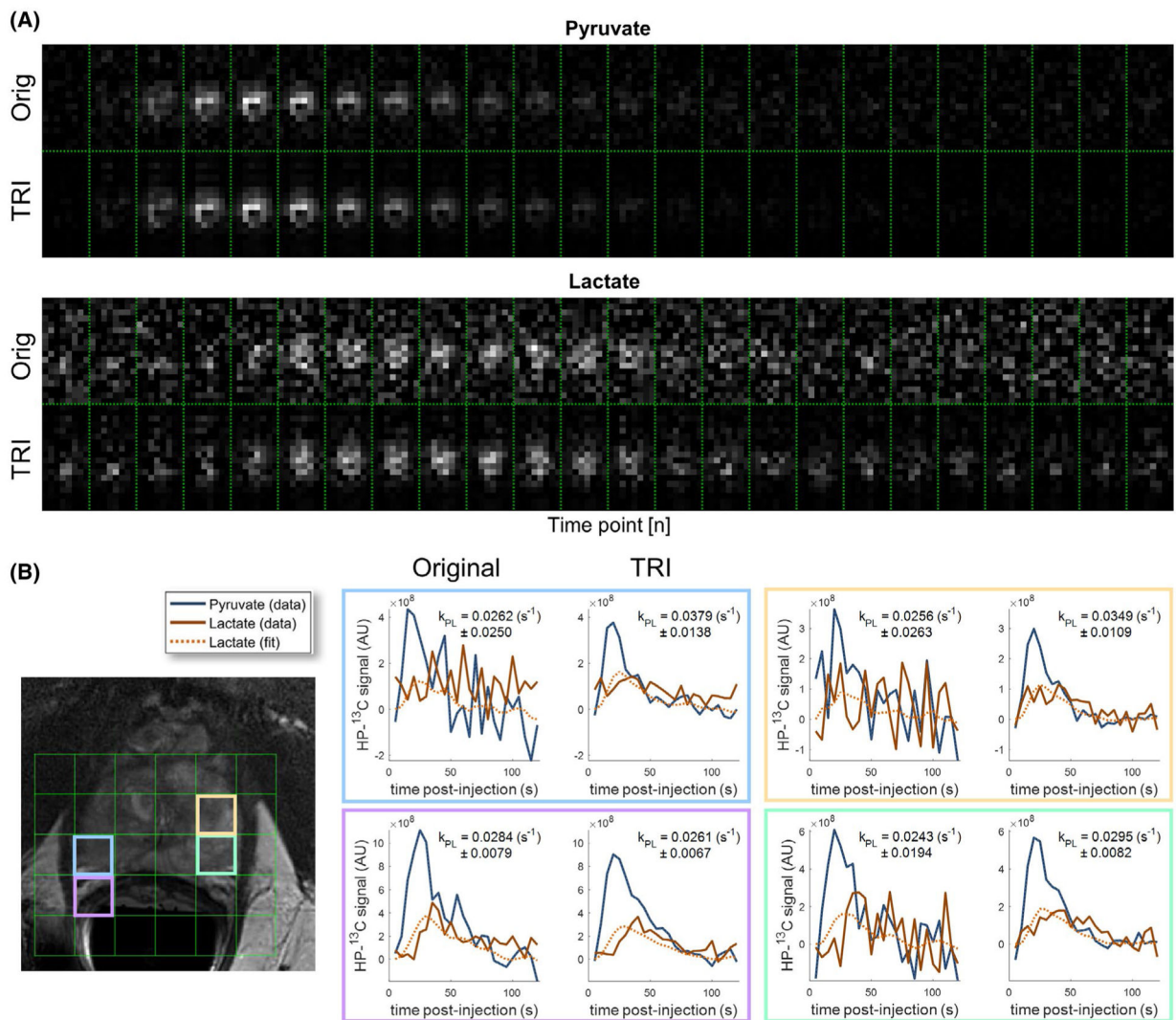
FIGURE 5.

This patient was diagnosed with bilateral biopsy-confirmed prostate cancer in left, right midgland and right apex. T_2-FSE (fast spin echo) images identified suspected lesions both in left and right midgland as low signal intensity (dark regions). The dynamic spectroscopy (green voxel) illustrated apparent signal-to-noise (aSNR) gains in pyruvate, lactate, and even recovery of the otherwise undetectable alanine and pyruvate hydrate

FIGURE 6.

Continuation of Figure 5. A, Dynamic series of pyruvate and lactate illustrated improved spatiotemporal characteristics, especially in lactate. Overall apparent signal-to-noise (aSNR) gain was 67-fold in this data set. B, Tensor Rank truncation-Image enhancement (TRI) provided better dynamic characteristic particularly for low-SNR lactate. This resulted in more reliable fits of pyruvate-to-lactate conversion k_{PL}. The error metrics were calculated as previously described.[30] The pathophysiological information, such as the prostate biopsy results, are provided post hoc to correlate with the TRI-processed data and played no role in rank selection
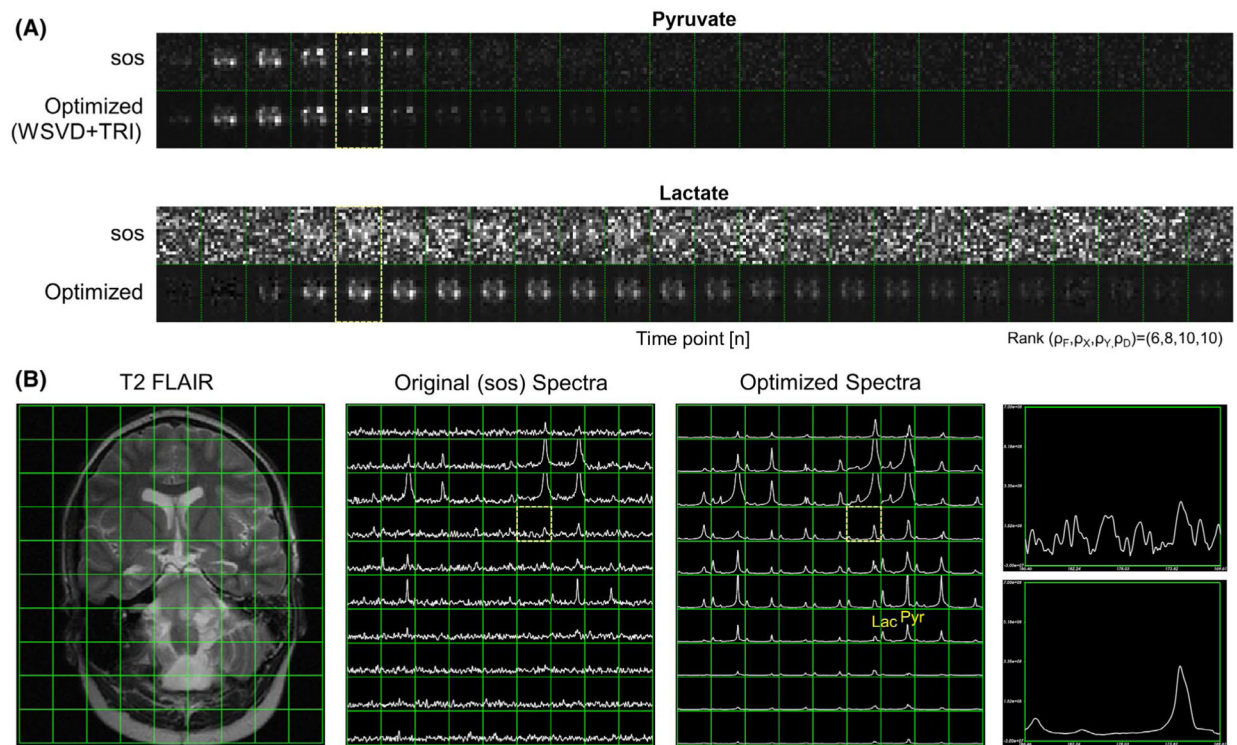
FIGURE 7.
Synergy of whitened singular value decomposition (WSVD) channel sum and Tensor Rank truncation-Image enhancement (TRI) in the improved processing workflow. A, This pediatric patient presented with diffuse intrinsic pontine glioma. The pediatric human hyperpolarized (HP)-^{13}C exams are notoriously challenging to perform due to their common localization near brainstem, limited injection dose, and rate. The original data (sum-of-squares) had relatively poor signal-to-noise ratio (SNR). Comparison between optimized data versus original found 597-fold apparent SNR gain. Upon closer examination, 7-fold SNR improvement was attributed to WSVD array combination, whereas 88-fold was due to TRI. B, Snapshot at time point 5 showed substantially improved spectral characteristics. Interestingly, even some spatial Gibbs ringing was "recovered"
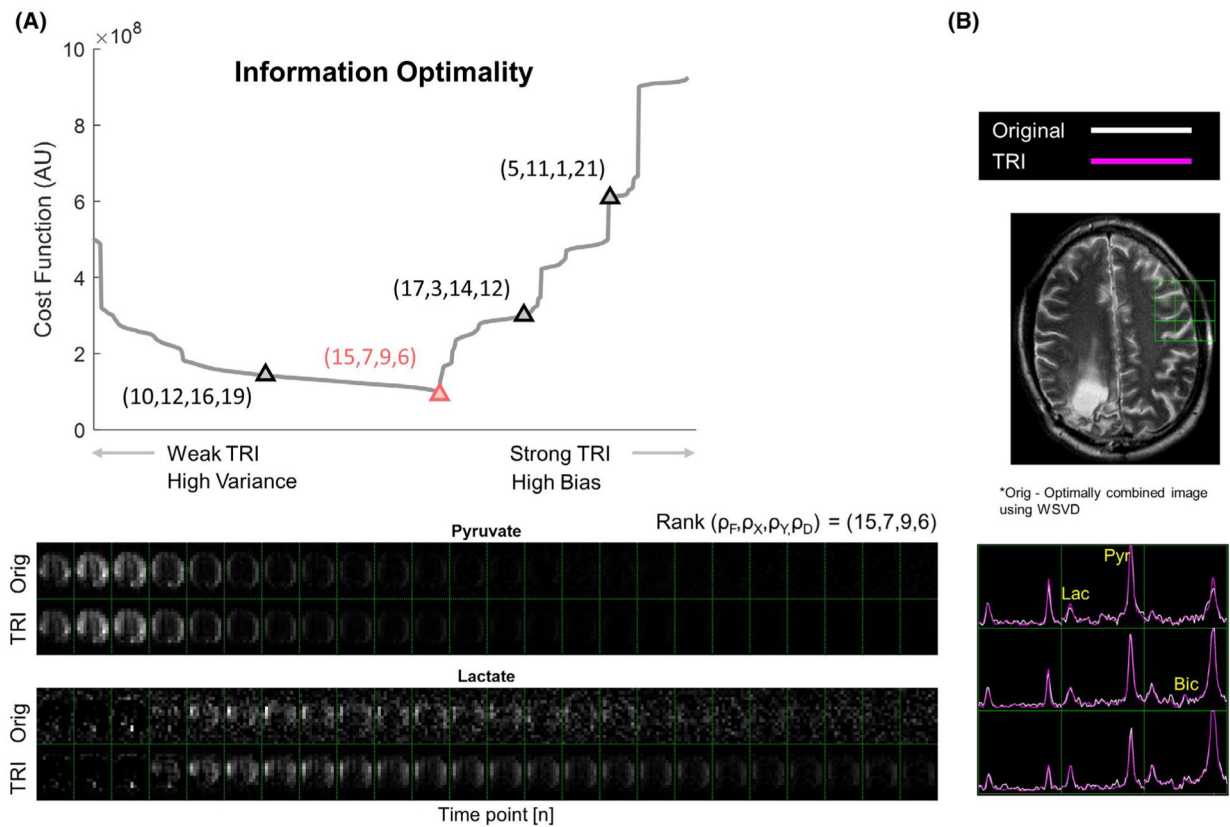
FIGURE 8.

A, Cost function with different degree of Tensor Rank truncation-Image enhancement (TRI). Weak TRI leads to higher variance, whereas strong TRI leads to higher bias. The optimality condition minimized cost function, defined as the sum of bias and variance. B, An illustration of bias-variance compromise using different ranks can be found in Supporting Information Figure 4. This shows TRI using rank determined by optimality criteria